Research Article | Vol. 31, No. 16 / 31 Jul 2023 / Optics Express 26591
Optics EXPRESS

Tunable chiral photonic cavity based on multiferroic layers

VAKHTANG JANDIERI,[1] RAMAZ KHOMERIKI,[2,*] KOKI WATANABE,[3] DANIEL ERNI,[1] DOUGLAS H. WERNER,[4] AND JAMAL BERAKDAR[5]

[1]*General and Theoretical Electrical Engineering (ATE), Faculty of Engineering, University of Duisburg-Essen and CENIDE —Center for Nanointegration Duisburg-Essen, D- 47048 Duisburg, Germany*
[2]*Physics Department, Tbilisi State University, 3 Chavchavadze, 0128 Tbilisi, Georgia*
[3]*Department of Information and Communication Engineering, Fukuoka Institute of Technology, 3-30-1 Wajirohigashi, Higashi-ku, Fukuoka 811-0295, Japan*
[4]*Department of Electrical Engineering, The Pennsylvania State University, University Park, PA 16802, USA*
[5]*Institut für Physik, Martin-Luther-Universität, Halle-Wittenberg, D-06099 Halle/Saale, Germany*
[*]*ramaz.khomeriki@tsu.ge*

Abstract: Realization of externally tunable chiral photonic sources and resonators is essential for studying and functionalizing chiral matter. Here, oxide-based stacks of helical multiferroic layers are shown to provide a suitable, electrically-controllable medium to efficiently trap and filter purely chiral photonic fields. Using analytical and rigorous coupled wave numerical methods we simulate the dispersion and scattering characteristics of electromagnetic waves in multiferroic heterostructures. The results evidence that due to scattering from the spin helix texture, only the modes with a particular transverse wavenumber form standing chiral waves in the cavity, whereas all other modes leak out from the resonator. An external static electric field enables a nonvolatile and energy-efficient control of the vector spin chirality associated with the oxide multilayers, which tunes the photonic chirality density in the resonator.

1. Introduction

Generation and control of chiral light is crucial for a number of applications in physics, chemistry, and biology [1–4] such as its use for enantiomeric selectivity [5]. An ability to control the enantiomeric ratio is, for example, important in medical drug production with increased therapeutic impact. Methods to generate chiral light [6] include the use of nanostructured metasurfaces [7] or the superposition of plane waves [8]. Confining chiral photonic fields, for instance in cavities, allows the light–matter interaction to be enhanced and offers a methodology to manipulate chiral dichroic effects [9,10]. Particularly useful are resonators with sizable chirality density that can be reversibly controlled by external fields with low-energy dissipation. Here, we exploit the spin-dependent scattering of light from the non-collinear spin texture in a helical multiferroic interface and show that a substantially large optical chiral density is formed between the interfaces. A suitable resonator material class was found to be dielectric multiferroic oxides with magnetically induced ferroelectricity such as RMn_2O_5 (R=Y,Ho,Bi) [11], $DyMnO_3$ [12], or $TbMnO_3$. In the helical phase, the ferroelectric polarization $\mathbf{P}$ is related to the helical spin order (due to an inverse Dzyaloshinskii-Moriya interaction) as indicated by the well-defined value of the vector spin chirality along the x-axis, $\kappa_{j,x} = (\mathbf{S_j} \times \mathbf{S_{j+1}})_x$ (where $\mathbf{S_j}$ describes the spin on site $\mathbf{j}$, as shown in Fig. 1). A collinear spin order implies $\kappa_{j,x} = 0$ and thus a vanishing $\mathbf{P}$, and vice versa. The intrinsic interactions responsible for this behavior include an interplay of spin-orbit coupling, crystal field effects, and electronic correlations [13–16]. Relevant to our study is the fact that an applied static electric field $\mathbf{E}_0$ contributes to the energy of the systems with $-\mathbf{E}_0 \cdot \mathbf{P}$ and can drive the system from the chiral phase to the collinear one [13], thus providing a mechanism to control spin-dependent scattering [17] by electric means and without driving charges or displacement

#489612 https://doi.org/10.1364/OE.489612
Journal © 2023 Received 9 Mar 2023; revised 1 Jul 2023; accepted 10 Jul 2023; published 26 Jul 2023

Optics EXPRESS

currents. Our goal is to clarify whether a region (with a thickness w) sandwiched between two helical multiferroic layers (cf. Fig. 1) would serve as resonator for chiral modes and whether the chiral density of the modes is sizable.

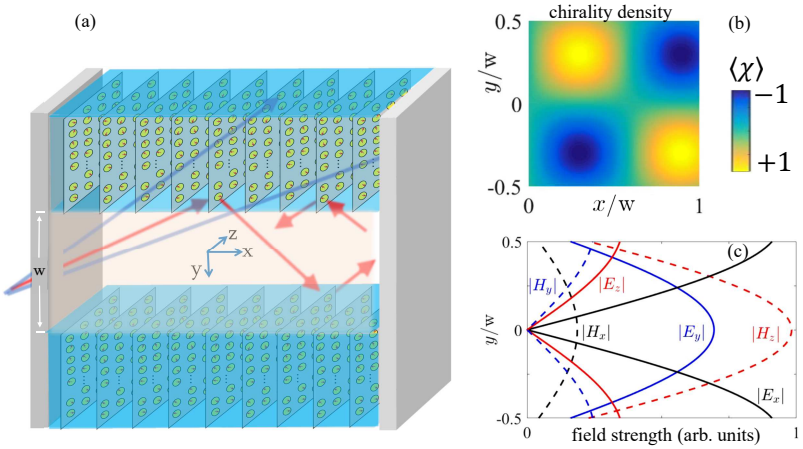

Fig. 1. (a) Schematic for an electrically controlled methodology for generating and confining purely chiral light between two chiral multiferroic multilayers. The modes are bounded by perfect mirrors attached to the left and right sides of the resonator, w is the thickness of the confining region. Radiative modes (blue arrows) leak out from the guiding region. Standing wave modes (red arrows) are purely chiral due to the spin-dependent scattering. (b) Time-averaged optical chiral density calculated using Eq. (8). (c) Electric and magnetic field strengths along the transverse y-axis for the normalized frequency $h/\lambda_0 = 0.1$ and a relative dielectric permittivity $\epsilon_r = 1.5$. The normalized propagation constant is equal to $k_x/k_0 = 0.706$ (calculated from the dispersion equation Eq. (5)). The fields are calculated using Eq. (7) together with Eq. (5).

Throughout the paper the overlined symbols indicate the matrices and the bold symbols indicate the vectors.

2. Formulation of the problem

We consider time-harmonic fields (with an angular frequency ω) entering the resonator at an incident angle ϕ_i measured from the positive x-axis (cf. Fig. 1). The wavevector characterizing the helical ordering Q is assumed to be the same for the upper and lower interface (Q is also referred to as the helicity index). The modes are bounded by perfect mirrors attached to the left and right sides of the resonator. Material studies [13,18] evidence that the local spins in the helical oxides are coupled antiferromagnetically (ferromagnetically) along the x-axis (z-axis), as indicated in the inset of Fig. 2. The helical ordering is along the y-axis. The length scales of the helical and antiferromegnetic order are set by $L = 2\pi/Q$ and h (inset in Fig. 2). By applying $\mathbf{E_0}$ along the z-axis, we can tune the helicity index Q. Namely, in the presence of the static electric field $\mathbf{E_0}$, the effective Dzyaloshinskii-Moriya vector constant is written as: $|\mathbf{D}| - g_{em}|\mathbf{E}_0|$, where g_{em} is the magnetoelectric coupling constant and $\mathbf{D}$ describes the antisymmetric exchange of the spins in the YOZ plane. Thus, with an applied static electric field one can tune the helicity index [17]. For $TbMnO_3$ the remnant helicity index (in case of zero applied electric field) is $Q_0 \simeq 0.28/a$, where a is an intralayer lattice constant. This means that $|\mathbf{D}| \simeq 0.3$ in units of exchange constant $J \approx 5$meV and taking $g_{em} \sim 20$ meV nm/V it appears that we can tune helicity index by applying electric field in the range of 1 V/nm.

Optics EXPRESS

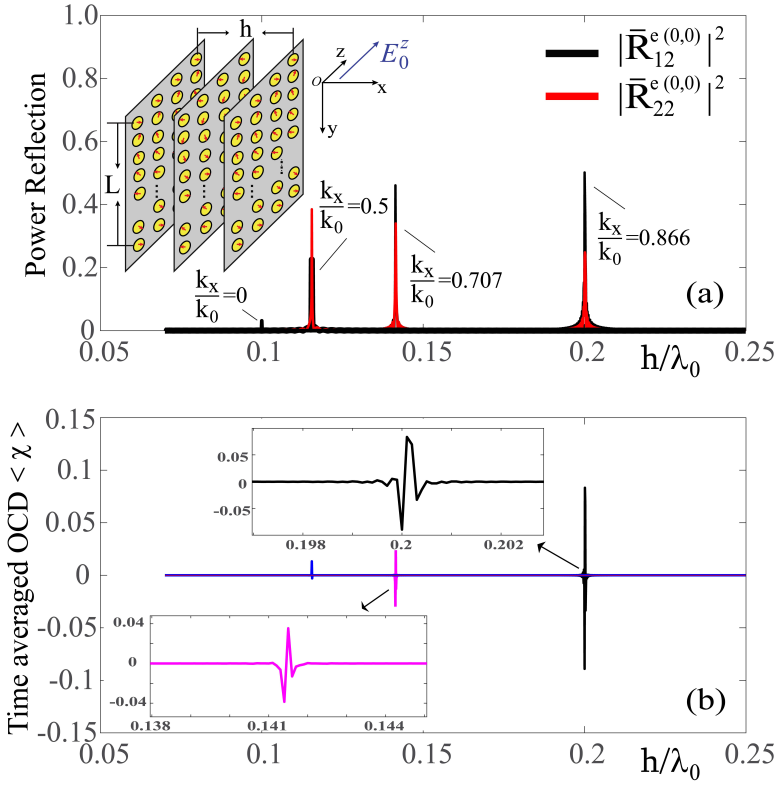

Fig. 2. (a) Power reflection of the fundamental (0,0) space harmonic of the electric field for a multiferroic material, which is used as an upper (lower) wall element for the resonator, versus h/λ_0 at different normalized values of the propagation constant k_x/k_0 when $\epsilon_r = 1.0$. TE wave incidence (E_z, H_x, H_y) is considered and from (S6) it follows that only (1,2) and (2,2) block matrices give a contribution in the formation of the fields. The details of the reflection matrices are given in Supplement 1. Inset shows a schematic of the considered unit cell of the sample with a spin-current driven helical spin order in the y-z plane and an antiferromagnetic ordering along the x-axis. The spin-driven ferroelectric polarization **P** is along the z-axis and can couple to an applied static electric field E_0^z, mediating an action of E_0^z on spin ordering. Here h is the lattice spacing (interlayer spacing) and L is the helical period. The thickness of the whole sample is $400L$, $L = 10h$ and $|\gamma|\mu_0 S_0 h/(2\pi c) = 0.009$. The helical step angle along the y-axis is equal to 36°, amounting to ten rotations within one period along the y-axis. (b) Time-averaged Optical Chiral Density (OCD) as a function of the normalized frequency h/λ_0 calculated using Eq. (6).

To capture the multiple scattering of electromagnetic waves due to the local, spin-dependent, dynamic response from the helical interfaces, we note the following. Quantum spin fluctuations are subsidiary (because of the relatively large magnetic moment, finite temperatures, and residual magnetic anisotropies). Therefore, we treat the coupled localized moments **S** classically. We are interested in scattering of waves with wavelength much larger than the interatomic distance and hence a continuum model for the dynamic of **S** is appropriate. The magnetic (**H**) and the electric (**E**) fields follow from the solution of the differential equations

$$\frac{\partial \mathbf{S}}{\partial t} = |\gamma|\mu_0 \left[\mathbf{S} \times \mathbf{H}\right], \tag{1}$$

Optics EXPRESS

$$\mu_0 \frac{\partial}{\partial t}[\mathbf{H} + \mathbf{S}] = -\nabla \times \mathbf{E}, \quad \epsilon_0 \epsilon_r \frac{\partial \mathbf{E}}{\partial t} = \nabla \times \mathbf{H}. \tag{2}$$

where γ is the gyromagnetic ratio, μ_0 (ϵ_0) is permeability (permittivity) of free space. The constant relative permittivity ϵ_r accounts for the background dielectric response of the multiferroic layers. The dielectric contribution due to $\mathbf{P}$ can be incorporated into the proposed formalism, however it is of less relevance for the magnetic response since $-\mathbf{E_0} \cdot \mathbf{P}$ is much smaller than the exchange interaction energies which govern the magnetic ordering [13].

Prior to the incident wave, the system resides in a stable ground state where the magnetic moments are ordered according to $\mathbf{S_0} = \mathbf{z}S_{0z}(x) + \mathbf{y}S_{0y}(x)$ in the layer, which we take as the $y-z$ plane. For a moderate amplitude of the incident wave it is sufficient to consider linear field-induced fluctuations $\mathbf{S_1}(x, y)$ around the ground state $\mathbf{S_0}$. The back action of $\mathbf{S_1}$ on the wave propagation determines $\mathbf{H}(x, y)$. Key to the findings presented below is the static chiral spin texture of the ground state $\mathbf{S_0}$ which varies on the scale of tens of nanometers [19]. Mathematically, Eqs. (1) and (2) provide a relation between the perturbed part of the spin magnetization density $\mathbf{S_1}(x, y)$ and the magnetic field $\mathbf{H}(x, y)$ in each spin grating layer. This relation is expressible through a relative permeability matrix $\overline{\overline{\mu}}(x)$ as $\mathbf{S_1}(x, y) = \overline{\overline{\mu}}(x)\mathbf{H}(x, y)$, where

$$\overline{\overline{\mu}}(x) = \begin{pmatrix} 0 & -i\mu_1(x) & i\mu_2(x) \\ i\mu_1(x) & 0 & 0 \\ -i\mu_2(x) & 0 & 0 \end{pmatrix}. \tag{3}$$

The position and frequency-dependent elements of the permeability tensor are given by $\mu_1(x) = |\gamma|\mu_0 S_{0z}(x)/\omega$ and $\mu_2(x) = |\gamma|\mu_0 S_{0y}(x)/\omega$. The multiple scattering between the electromagnetic waves and the magnetic material is encompassed in the relative permeability matrix $\overline{\overline{\mu}}$. To obtain the resulting modes, we apply the rigorous coupled-wave method (RCWM) [20]. The x, y and z components of the electromagnetic fields are pseudoperiodic functions of x with a period h and can be approximately expanded in a truncated Fourier series as

$$\begin{bmatrix} \mathbf{E}(x, y) \\ \mathbf{H}(x, y) \end{bmatrix} = \sum_{n=-N}^{N} \begin{bmatrix} \mathbf{e}_n(y) \\ \mathbf{h}_n(y) \end{bmatrix} e^{i(k_x + 2\pi n/h)x}, \tag{4}$$

where k_x is a propagation constant and N is a truncation number associated with the Fourier series. Note that the Fourier coefficients are functions only of y. Below, we consider simulations with truncation number $N = 4$ that obey the energy conservation.

Substituting Eqs. (3) and (4) into Eq. (2) and expressing the y component of the electric and magnetic fields in terms of the x and z components of the fields, a set of coupled differential equations is obtained. Technical derivations are given in Supplement 1, where it is also shown how the reflection matrices for anisotropic layers are inferred [21,22].

Having the generalized reflection matrix $\overline{\mathbf{R}}$ for a multilayered multiferroic structure shown as inset in Fig. 2 (see Supplement 1), the eigenmodes for the resonance structure (Fig. 1) are deduced from the dispersion equation

$$\det[\bar{\mathbf{I}} - \overline{\mathbf{W}}(k_x) \cdot \overline{\mathbf{R}}(k_x) \cdot \overline{\mathbf{W}}(k_x) \cdot \overline{\mathbf{R}}(k_x)] = \mathbf{0} \tag{5}$$

where $k_{yn} = \sqrt{k_0^2 - (k_x + 2\pi n/h)^2}$ is a wavenumber along the transverse y-axis for the n-th space-harmonic, k_0 is the wavenumber in a free space, $\bar{\mathbf{I}}$ is the unit matrix, $\overline{\mathbf{W}} = [\exp(-jk_{yn}w)\delta_{nm}]$ is a diagonal matrix, which represents the transverse travelling wave behaviour of the space-harmonics in the region having a thickness w. After the propagation constant k_x is explicitly found from Eq. (5), the electric and magnetic fields in the region with a thickness w (see Fig. 1)

Optics EXPRESS

are expressed through the amplitude column vectors $\mathbf{a}^{\pm} = (\mathbf{a}^{\pm}_{\mathbf{e_x}}, \mathbf{a}^{\pm}_{\mathbf{e_y}}, \mathbf{a}^{\pm}_{\mathbf{e_z}})$ and $\mathbf{b}^{\pm} = (\mathbf{b}^{\pm}_{\mathbf{h_x}}, \mathbf{b}^{\pm}_{\mathbf{h_y}}, \mathbf{b}^{\pm}_{\mathbf{h_z}})$, where $\mathbf{a}^{\pm}$ and $\mathbf{b}^{\pm}$ denote the up-going (+) and down-going (−) Floquet modes in the y direction for the electric and magnetic field components, respectively. The vectors $\mathbf{a}^{\pm}$ and $\mathbf{b}^{\pm}$ are the eigenvectors corresponding to the eigenvalues k_x/k_0 found using Eq. (5). Numerical investigations have shown that the up-going (+) and down-going (−) modes are connected by the following relations: $\mathbf{a}^{+}_{\mathbf{e_x}} = -\mathbf{a}^{-}_{\mathbf{e_x}}$, $\mathbf{a}^{+}_{\mathbf{e_y}} = \mathbf{a}^{-}_{\mathbf{e_y}}$, $\mathbf{a}^{+}_{\mathbf{e_z}} = -\mathbf{a}^{-}_{\mathbf{e_z}}$, $\mathbf{b}^{+}_{h_x} = \mathbf{b}^{-}_{h_x}$, $\mathbf{b}^{+}_{h_y} = -\mathbf{b}^{-}_{h_y}$, $\mathbf{b}^{+}_{h_z} = \mathbf{b}^{-}_{h_z}$ and, thus they are characterized by opposite chirality density according to

$$\langle \chi \rangle = \frac{h}{\lambda_0} \Im(\mathbf{E} \cdot \tilde{\mathbf{H}}^{*}) \tag{6}$$

where $\langle \chi \rangle$ is normalized by $\pi\epsilon_0/h$ (Figs. 2 and 3). Reflection from the left and right-side mirrors of the resonator leads to a change in the chirality density (see Fig. 1). Under the prescribed parameters only the 0-th space-harmonic contributes to the formation of the fields in the region $|y| < w/2$. Thus, the fields can be written in the following simple form

$$\begin{aligned} E_x &= a^{+}_{e_x} \sin(k_y y)\cos(k_x x), \quad & E_y &= a^{+}_{e_y} \cos(k_y y)\sin(k_x x), \\ E_z &= a^{+}_{e_z} \sin(k_y y)\sin(k_x x), \quad & H_x &= b^{+}_{h_x} \cos(k_y y)\sin(k_x x), \\ H_y &= b^{+}_{h_y} \sin(k_y y)\cos(k_x x), \quad & H_z &= b^{+}_{h_z} \cos(k_y y)\cos(k_x x). \end{aligned} \tag{7}$$

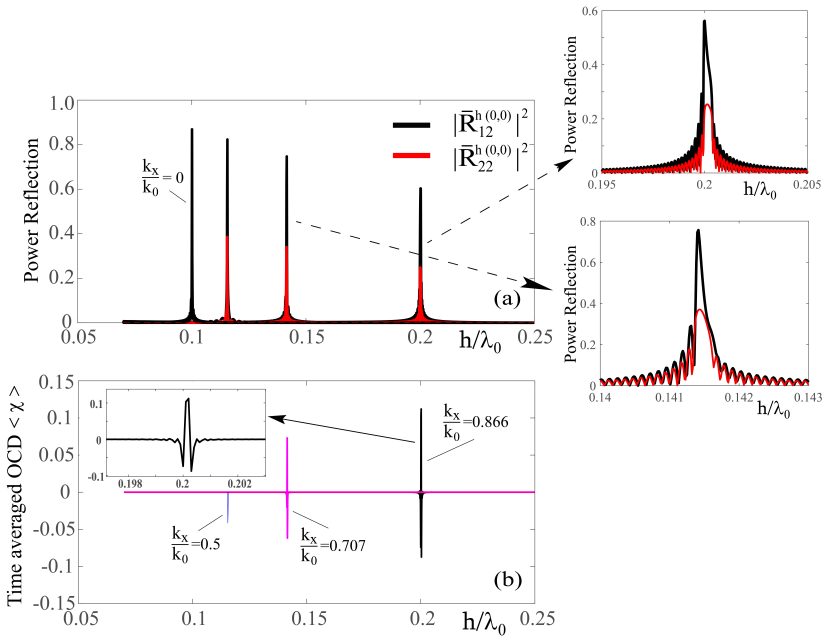

Fig. 3. The same as in Fig. 2 but for the reflected magnetic field at TM wave incidence (H_z, E_x, E_y). For these simulations we use Eq. (6) together with (Supplement 1, S7).

For the optical chirality density we infer

$$\langle \chi \rangle = \frac{h}{\lambda_0} \Im[\mathbf{a}^{+} \cdot (\mathbf{b}^{+})^{*}] \sin(2k_x x)\sin(2k_y y). \tag{8}$$

Note that in Fig. 1(b) the chiral density is normalized to its maximum value at the fixed normalized frequency h/λ_0. No achiral modes are allowed in the resonator.

Optics EXPRESS

3. Numerical results and discussions

For an estimation of the magnitude of the chirality of the fields in the resonator, we consider a resonator thickness $w = 6h$ and plot the absolute values of the fields along the y-axis in Fig. 1(c). The chirality density pattern calculated using Eq. (8) is shown in Fig. 1(b). The normalized frequency is fixed at $h/\lambda_0 = 0.1$ when $\epsilon_r = 1.5$, and the propagation constant $k_x/k_0 = 0.706$ is calculated from Eq. (5). The thickness of the helical antiferromagnetic structure (cf. inset in Fig. 2(a)) is $400L$, $L = 10h$ and L is the helical period. A helical step angle along the y-axis is equal to 36° (i.e., ten rotations within one period of L). We find that the phase differences between the electric and magnetic fields do not change within the region $0 < y < w/2$. Photonic fields with nonzero chirality are formed in regions where the electric field has a finite, out of phase component along the magnetic field. This is the case everywhere in the guiding region $|y| < w/2$.

To investigate in a detail a formation for the chiral fields in the resonator (Fig. 1(a)), firstly, it is necessary to study the scattering characteristics, namely the reflection of a multiferroic material, which is used as an upper (lower) wall element for the resonator. The power reflections of a helical antiferromagnetic structure versus the normalized frequency h/λ_0 in the case of TE (E_z, H_x, H_y) and TM (H_z, E_x, E_y) wave incidences are shown in Figs. 2(a) and 3(a), respectively, for different values of the normalized propagation constant k_x/k_0: $k_x/k_0 = 0.866$, $k_x/k_0 = 0.707$, $k_x/k_0 = 0.5$ and $k_x/k_0 = 0.0$. Note, $k_x/k_0 \approx \cos(\phi_i)$, where ϕ_i is the angle of incidence [17]. Only the (0,0) component of the block matrices $\overline{\mathbf{R}}_{12}$ and $\overline{\mathbf{R}}_{22}$ are plotted as the dotted and solid lines, respectively. These block matrices give a contribution in the formation of the fields as it is shown in (S6) and (S7) in Supplement 1. Sharp resonances appear at particular frequencies, whereas at other frequencies the sample is completely transparent. The time averaged optical chiral densities are depicted in Figs. 2(b) and 3(b). The values of $\langle \chi \rangle$ are decreasing proportionally to the normalized propagation constant. At $k_x/k_0 = 0$, the cross diagonal matrix $\overline{\mathbf{R}}_{12}$ elements become zero (see Figs. 2(a) and 3(a)), which is equivalent to the simple model corresponding to isotropic media and hence, a field with non-vanishing optical chirality is not formed. The results in Figs. 2 and 3 have been calculated for $\epsilon_r = 1$.

By increasing the relative dielectric permittivity ϵ_r, the sharp resonance peaks in Figs. 2 and 3 are shifted to lower frequencies. Using our analytical derivations, by varying the relative dielectric permittivity ϵ_r, the new peaks should be observed at the frequencies f_s defined as

$$f_s = f\,(k_x/k_0)/\sqrt{\epsilon_r - 1 + (k_x/k_0)^2} \tag{9}$$

where f is a frequency where the resonance peak is formed at the fixed value of k_x/k_0 when $\epsilon_r = 1$ (see Figs. 2 and 3). The correctness of Eq. (9) has been validated numerically. In particular, at $\epsilon_r = 1.5$ and $k_x/k_0 = 0.707$, the resonance peak (in Figs. 2 and 3) is shifted to the lower frequency $f_s = h/\lambda_0 = 0.1$. This is the frequency at which simulations for the chiral field resonator are performed (see Fig. 1).

An important feature of our resonator is that the helicity index Q can be controlled by a static applied electric field E_0^z. For a fixed excitation frequency h/λ_0 and keeping the material parameters the same, the normalized propagation constant k_x/k_0 can be uniquely controlled only by an applied electric field. Decreasing the helicity index Q results in a smoothing of the noncollinear ordering of the multiferroic material. The ratio of the helical indices Q_1 and Q_2 is analytically expressed through the propagation constant in the following form

$$\frac{Q_1}{Q_2} = \frac{\sqrt{1 - (k_x/k_0)^2_{Q_1}}}{\sqrt{1 - (k_x/k_0)^2_{Q_2}}} \tag{10}$$

where $(k_x/k_0)_{Q_1}$ and $(k_x/k_0)_{Q_2}$ are the propagation constants with fixed helical indices Q_1 and Q_2, respectively. Numerically we find that at a helical step angle along the y-axis equal to 18° (i.e.,

Optics EXPRESS

20 rotations within one period L along the y-axis), at the fixed normalized frequency $h/\lambda_0 = 0.1$, the propagation constant is $k_x/k_0 = 0.866$. For comparison, at the same normalized frequency but for a higher helicity index Q, as it is shown in Figs. 2 and 3, the propagation constant is equal to $k_x/k_0 = 0$. Further results indicate that a favorable setting for eigenmode formation is when $w \geq L/2$. When varying the resonator thickness within $L/2 < w < L$, the simulations show that the propagation constant does not exhibit any noticeable changes. For a helical period around $L = 100$ nm [19], the thickness of the resonator can be in the range of 70 nm.

4. Conclusion

In summary, layers of helical multiferroic oxides provide a suitable platform for trapping and electrically controlling chiral photonic fields adding a new twist to the field of oxide and perovskite-based photonics [23–31]. Structurally and electronically the above discussed material class combines well with other ferroelastic or ferroelectric materials such as $BaTiO_3$ [32] and exhibits multiple phases as a function of external parameters such as temperature, pressure and electric gates pointing to potential use in sensoric and material characterization.

Funding. Deutsche Forschungsgemeinschaft (287022738, 429194455).

Acknowledgement. This work has been supported (J.B.) by the Deutsche Forschungsgemeinschaft (DFG) under Project Nr. 429194455. D.E. and V.J. acknowledge the partial support by DFG under Project 287022738 CRC/TRR 196 MARIE (Project M03).

Disclosures. The authors declare no conflicts of interest.

Data availability. Data underlying the results presented in this paper are not publicly available at this time but may be obtained from the authors upon reasonable request.

Supplemental document. See Supplement 1 for supporting content.

References

1. Y. Tang and A. E. Cohen, "Optical chirality and its interaction with matter," Phys. Rev. Lett. **104**(16), 163901 (2010).
2. K. Y. Bliokh and F. Nori, "Characterizing optical chirality," Phys. Rev. A **83**(2), 021803 (2011).
3. M. P. Silverman, "Reflection and refraction at the surface of a chiral medium: comparison of gyrotropic constitutive relations invariant or noninvariant under a duality transformation," J. Opt. Soc. Am. A **3**(6), 830 (1986).
4. E. U. Condon, "Theories of optical rotatory power," Rev. Mod. Phys. **9**(4), 432–457 (1937).
5. C. Genet, "Chiral light–chiral matter interactions: an optical force perspective," ACS Photonics **9**(2), 319–332 (2022).
6. J. Mun, M. Kim, Y. Yang, T. Badloe, J. Ni, Y. Chen, C.-W. Qiu, and J. Rho, "Electromagnetic chirality: from fundamentals to nontraditional chiroptical phenomena," Light: Sci. Appl. **9**(1), 139 (2020).
7. D. Schulz, B. Schwager, and J. Berakdar, "Nanostructured spintronic emitters for polarization-textured and chiral broadband THz fields," ACS Photonics **9**(4), 1248–1255 (2022).
8. J. Zhang, S. Huang, Z. Lin, and J. Huang, "Generation of optical chirality patterns with plane waves, evanescent waves and surface plasmon waves," Opt. Express **28**(1), 760–772 (2020).
9. A. O. Govorov, Z. Fan, P. Hernandez, J. M. Slocik, and R. R. Naik, "Theory of circular dichroism of nanomaterials comprising chiral molecules and nanocrystals: plasmon enhancement, dipole interactions, and dielectric effects," Nano Lett. **10**(4), 1374–1382 (2010).
10. I. Fernandez-Corbaton, M. Fruhnert, and C. Rockstuhl, "Objects of maximum electromagnetic chirality," Phys. Rev. X **6**(3), 031013 (2016).
11. S.-W. Cheong and M. Mostovoy, "Multiferroics: a magnetic twist for ferroelectricity," Nat. Mater. **6**(1), 13–20 (2007).
12. F. Kagawa, M. Mochizuki, Y. Onose, H. Murakawa, Y. Kaneko, N. Furukawa, and Y. Tokura, "Dynamics of multiferroic domain wall in spin-cycloidal ferroelectric $DyMnO_3$," Phys. Rev. Lett. **102**(5), 057604 (2009).
13. M. Fiebig, Th. Lottermoser, D. Meier, and M. Trassin, "The evolution of multiferroics," Nat. Rev. Mater. **1**(8), 16046 (2016).
14. H. Katsura, N. Nagaosa, and A. V. Balatsky, "Spin current and magnetoelectric effect in noncollinear magnets," Phys. Rev. Lett. **95**(5), 057205 (2005).
15. M. Mostovoy, "Ferroelectricity in spiral magnets," Phys. Rev. Lett. **96**(6), 067601 (2006).
16. C. Jia, S. Onoda, N. Nagaosa, and J. H. Han, "Microscopic theory of spin-polarization coupling in multiferroic transition metal oxides," Phys. Rev. B **76**(14), 144424 (2007).
17. V. Jandieri, R. Khomeriki, L. Chotorlishvili, K. Watanabe, D. Erni, D. H. Werner, and J. Berakdar, "Photonic signatures of spin-driven ferroelectricity in multiferroic dielectric oxides," Phys. Rev. Lett. **127**(12), 127601 (2021).
18. L. Ponet, S. Artyukhin, Th. Kain, J. Wettstein, A. Pimenov, A. Shuvaev, X. Wang, S.-W. Cheong, M. Mostovoy, and A. Pimenov, "Topologically protected magnetoelectric switching in a multiferroic," Nature **607**(7917), 81–85 (2022).

Optics EXPRESS

19. R. D. Johnson, L. C. Chapon, D. D. Khalyavin, P. Manuel, P. G. Radaelli, and C. Martin, "Giant improper ferroelectricity in the ferroaxial magnet $CaMn_7O_{12}$," Phys. Rev. Lett. **108**(6), 067201 (2012).
20. K. Watanabe, "Numerical integration schemes used on the differential theory for anisotropic gratings," J. Opt. Soc. Am. A **19**(11), 2245–2252 (2002).
21. V. Jandieri, P. Baccarelli, G. Valerio, and G. Schettini, "1-D periodic lattice sums for complex and leaky waves in 2-D structures using higher order Ewald formulation," IEEE Trans. Antennas Propag. **67**(4), 2364–2378 (2019).
22. K. Yasumoto, *Electromagnetic Theory and Applications for Photonic Crystals* (Boca Raton, FL: CRC Press, 2005).
23. C. Xiong, W. H. P. Pernice, J. H. Ngai, J. W. Reiner, D. Kumah, F. J. Walker, C. H. Ahn, and H. X. Tang, "Active silicon integrated nanophotonics: ferroelectric $BaTiO_3$ devices," Nano Lett. **14**(3), 1419–1425 (2014).
24. J. E. Ortmann, M. R. McCartney, A. Posadas, D. J. Smith, and A. A. Demkov, "Epitaxial oxides on glass: a platform for integrated oxide devices," ACS Appl. Nano Mater. **2**(12), 7713–7718 (2019).
25. T. Jin, L. Li, B. Zhang, Hao-Yu, G. Lin, H. Wang, and P. T. Lin, "Monolithic mid-infrared integrated photonics using silicon-on-epitaxial barium titanate thin films," ACS Appl. Mater. Interfaces **9**(26), 21848–21855 (2017).
26. F. Eltes, D. Caimi, F. Fallegger, M. Sousa, E. O'Connor, M. D. Rossell, B. Offrein, J. Fompeyrine, and S. Abel, "Low-loss $BaTiO_3$–Si waveguides for nonlinear integrated photonics," ACS Photonics **3**(9), 1698–1703 (2016).
27. A. Karvounis, F. Timpu, V. V. Vogler-Neuling, R. Savo, and R. Grange, "Barium titanate nanostructures and thin films for photonics," Adv. Opt. Mater. **8**(24), 2001249 (2020).
28. A. Karvounis, V. V. Vogler-Neuling, F. U. Richter, E. Dénervaud, M. Timofeeva, and R. Grange, "Electro-optic metasurfaces based on barium titanate nanoparticle films," Adv. Opt. Mater. **8**(17), 2000623 (2020).
29. M. Duncan, J. E. Ortmann, and A. A. Demkov, "Dynamic waveguiding in Silicon-integrated barium titanate thin films," *2019 IEEE MTT-S International Conference on Numerical Electromagnetic and Multiphysics Modeling and Optimization (NEMO)*, 1–4 (2019).
30. R. Khomeriki, L. Chotorlishvili, I. Tralle, and J. Berakdar, "Positive–negative birefringence in multiferroic layered metasurfaces," Nano Lett. **16**(11), 7290–7294 (2016).
31. S. Abel, F. Eltes, and J. E. Ortmann, *et al.*, "Large Pockels effect in micro- and nanostructured barium titanate integrated on silicon," Nat. Mater. **18**(1), 42–47 (2019).
32. M. Acosta, N. Novak, V. Rojas, S. Patel, R. Vaish, J. Koruza, Jr. G. A. Rossetti, and J. Rödel, "$BaTiO_3$-based piezoelectrics: Fundamentals, current status, and perspectives," Appl. Phys. Rev. **4**(4), 041305 (2017).

Supplemental Document

Optics EXPRESS

Tunable chiral photonic cavity based on multiferroic layers: supplement

VAKHTANG JANDIERI,[1] RAMAZ KHOMERIKI,[2,*] KOKI WATANABE,[3] DANIEL ERNI,[1] DOUGLAS H. WERNER,[4] AND JAMAL BERAKDAR[5]

[1]*General and Theoretical Electrical Engineering (ATE), Faculty of Engineering, University of Duisburg-Essen and CENIDE —Center for Nanointegration Duisburg-Essen, D- 47048 Duisburg, Germany*
[2]*Physics Department, Tbilisi State University, 3 Chavchavadze, 0128 Tbilisi, Georgia*
[3]*Department of Information and Communication Engineering, Fukuoka Institute of Technology, 3-30-1 Wajirohigashi, Higashi-ku, Fukuoka 811-0295, Japan*
[4]*Department of Electrical Engineering, The Pennsylvania State University, University Park, PA 16802, USA*
[5]*Institut für Physik, Martin-Luther-Universität, Halle-Wittenberg, D-06099 Halle/Saale, Germany*
[*]*ramaz.khomeriki@tsu.ge*

Supplement DOI: https://doi.org/10.6084/m9.figshare.23674392

Parent Article DOI: https://doi.org/10.1364/OE.489612

Tunable chiral photonic cavity based on multiferroic layers

In the main text, substituting Eqs.(3) and (4) into Eq.(2), it follows that the relation between the Fourier coefficients can be written in the following form

$$
\begin{aligned}
&\frac{\mathrm{d}}{\mathrm{d}y}h_z(y) = -ik_0[\![1/\varepsilon_r]\!]^{-1}e_x(y)\\
&\overline{\mathbf{K}}h_z(y) = [\![\varepsilon_r]\!]e_y(y)\\
&ik_0\overline{\mathbf{K}}h_y(y) - \frac{\mathrm{d}}{\mathrm{d}y}h_x(y) = -ik_0[\![\varepsilon_r]\!]e_z(y)\\
&\frac{\mathrm{d}}{\mathrm{d}y}e_z(y) = ik_0\left(h_x(y) - i\,[\![\mu_1]\!]h_y(y) + i[\![\mu_2]\!]h_z(y)\right)\\
&-\overline{\mathbf{K}}e_z(y) = i[\![\mu_1]\!]h_x(y) + \left(\bar{\mathbf{I}} + [\![\mu_1]\!]^2 - [\![{\mu_1}^2]\!]\right)h_y(y)\\
&\qquad -\left([\![\mu_1]\!]\,[\![\mu_2]\!] - [\![\mu_1\,\mu_2]\!]\right)h_z(y)\\
&ik_0\overline{\mathbf{K}}e_y(y) - \frac{\mathrm{d}}{\mathrm{d}y}e_x(y) = ik_0[-i[\![\mu_2]\!]h_x(y) -\\
&\left([\![\mu_2]\!]\,[\![\mu_1]\!] - [\![\mu_1\,\mu_2]\!]\right)h_y(y) + \left(\bar{\mathbf{I}} + [\![\mu_2]\!]^2 - [\![{\mu_2}^2]\!]\right)h_z(y)]
\end{aligned}
\tag{S1}
$$

with

$$
[\![\mathrm{Y}]\!]_{n,m} = \frac{1}{h}\int_0^h \mathrm{Y}(x)e^{-i(n-m)2\pi x/h}dx, \quad \mathrm{Y} = [\mu_1, \mu_2, \varepsilon_r] \tag{S2}
$$

$$
(\overline{\mathbf{K}})_{n,m} = [k_{xn}\delta_{n,m}] = \delta_{n,m}\Big(\frac{k_x}{k_0} + \frac{2\pi n}{hk_0}\Big) \tag{S3}
$$

Here k_0 is the free-space wavenumber, $[\![\mathrm{Y}]\!]$ is a square Toeplitz matrix generated by the Fourier coefficients of Y with the (n, m) entries equal to Y_{n-m}.

Expressing the y component of the electric and magnetic fields in terms of the x and z components, Maxwell's equations can be transformed into the following coupled differential equations [1]

$$
\frac{\mathrm{d}}{\mathrm{d}y}\begin{pmatrix} e_x(y)\\ e_z(y)\\ \tilde{h}_x(y)\\ \tilde{h}_z(y)\end{pmatrix} = ik_0\begin{pmatrix} 0 & M_{12} & M_{13} & M_{14}\\ 0 & M_{22} & M_{23} & M_{24}\\ 0 & M_{32} & M_{33} & M_{34}\\ M_{41} & 0 & 0 & 0\end{pmatrix}\begin{pmatrix} e_x(y)\\ e_z(y)\\ \tilde{h}_x(y)\\ \tilde{h}_z(y)\end{pmatrix} \tag{S4}
$$

with

$$
\begin{aligned}
M_{12} &= -\left(\llbracket\mu_2\rrbracket\,\llbracket\mu_1\rrbracket - \llbracket\mu_1\,\mu_2\rrbracket\right)\left(\bar{\mathbf{I}} + \llbracket\mu_1\rrbracket^2 - \llbracket{\mu_1}^2\rrbracket\right)^{-1}\overline{\mathbf{K}} \\
M_{13} &= i[\llbracket\mu_2\rrbracket - (\llbracket\mu_2\rrbracket\,\llbracket\mu_1\rrbracket - \llbracket\mu_1\,\mu_2\rrbracket) \\
&\quad (\bar{\mathbf{I}} + \llbracket\mu_1\rrbracket^2 - \llbracket{\mu_1}^2\rrbracket)^{-1}\,\llbracket\mu_1\rrbracket] \\
M_{14} &= -\bar{\mathbf{I}} + \overline{\mathbf{K}}\llbracket\varepsilon_r\rrbracket^{-1}\overline{\mathbf{K}} - \llbracket\mu_2\rrbracket^2 + \llbracket{\mu_2}^2\rrbracket \\
&\quad + (\llbracket\mu_2\rrbracket\,\llbracket\mu_1\rrbracket - \llbracket\mu_1\,\mu_2\rrbracket)(\bar{\mathbf{I}} + \llbracket\mu_1\rrbracket^2 - \llbracket{\mu_1}^2\rrbracket)^{-1} \\
&\quad (\llbracket\mu_1\rrbracket\,\llbracket\mu_2\rrbracket - \llbracket\mu_1\,\mu_2\rrbracket) \\
M_{22} &= i\,\llbracket\mu_1\rrbracket\left(\bar{\mathbf{I}} + \llbracket\mu_1\rrbracket^2 - \llbracket{\mu_1}^2\rrbracket\right)^{-1}\overline{\mathbf{K}} \\
M_{23} &= \bar{\mathbf{I}} - \llbracket\mu_1\rrbracket(\bar{\mathbf{I}} + \llbracket\mu_1\rrbracket^2 - [{\mu_1}^2])^{-1}\,\llbracket\mu_1\rrbracket \\
M_{24} &= i[\llbracket\mu_2\rrbracket - \llbracket\mu_1\rrbracket(\bar{\mathbf{I}} + \llbracket\mu_1\rrbracket^2 - \llbracket{\mu_1}^2\rrbracket)^{-1} \\
&\quad (\llbracket\mu_1\rrbracket\,\llbracket\mu_2\rrbracket - \llbracket\mu_1\,\mu_2\rrbracket)] \\
M_{32} &= \llbracket\varepsilon_r\rrbracket - \overline{\mathbf{K}}\left(\bar{\mathbf{I}} + \llbracket\mu_1\rrbracket^2 - \llbracket{\mu_1}^2\rrbracket\right)^{-1}\overline{\mathbf{K}} \\
M_{33} &= -i\,\overline{\mathbf{K}}\left(\bar{\mathbf{I}} + \llbracket\mu_1\rrbracket^2 - \llbracket{\mu_1}^2\rrbracket\right)^{-1}\llbracket\mu_1\rrbracket \\
M_{34} &= \overline{\mathbf{K}}\left(\bar{\mathbf{I}} + \llbracket\mu_1\rrbracket^2 - \llbracket{\mu_1}^2\rrbracket\right)^{-1}(\llbracket\mu_1\rrbracket\,\llbracket\mu_2\rrbracket - \llbracket\mu_1\,\mu_2\rrbracket) \\
M_{41} &= -\llbracket 1/\varepsilon_r\rrbracket^{-1}
\end{aligned}
\tag{S5}
$$

Here $\tilde{\mathbf{h}}_{x,z}(y)=\sqrt{\mu_0/\epsilon_0}\,\mathbf{h}_{x,z}(y)$, $\bar{\mathbf{I}}$ is the unit matrix and $\delta_{n,m}$ is the Kronecker's delta function.

The reflection and transmission matrices for a single anisotropic layer can be calculated using Eqs.(S4) and (S5) [1] . When the grating is multilayered, the transmitted waves from a single layer impinge on the nearest layer as new incident waves and are scattered into another set of space-harmonics [2, 3]. The multiple interaction process between the anisotropic layers can be described by applying the scattering matrix (S-matrix) propagation algorithm and the amplitude vectors for the reflected electric $(\mathbf{e}_x^r, \mathbf{e}_z^r)$ and magnetic $(\tilde{\mathbf{h}}_x^r, \tilde{\mathbf{h}}_z^r)$ fields can be defined through the incident field amplitudes $(\mathbf{e}_x^i, \mathbf{e}_z^i)$, $(\tilde{\mathbf{h}}_x^i, \tilde{\mathbf{h}}_z^i)$ in the following form:

$$
\begin{bmatrix}\mathbf{e}_x^r\\ \mathbf{e}_z^r\end{bmatrix} = \overline{\mathbf{R}}^e\begin{bmatrix}\mathbf{e}_x^i\\ \mathbf{e}_z^i\end{bmatrix} = \begin{bmatrix}\overline{\mathbf{R}}_{11}^e & \overline{\mathbf{R}}_{12}^e\\ \overline{\mathbf{R}}_{21}^e & \overline{\mathbf{R}}_{22}^e\end{bmatrix}\begin{bmatrix}\mathbf{e}_x^i\\ \mathbf{e}_z^i\end{bmatrix} \tag{S6}
$$

$$
\begin{bmatrix}\tilde{\mathbf{h}}_x^r\\ \tilde{\mathbf{h}}_z^r\end{bmatrix} = \overline{\mathbf{R}}^h\begin{bmatrix}\tilde{\mathbf{h}}_x^i\\ \tilde{\mathbf{h}}_z^i\end{bmatrix} = \begin{bmatrix}\overline{\mathbf{R}}_{11}^h & \overline{\mathbf{R}}_{12}^h\\ \overline{\mathbf{R}}_{21}^h & \overline{\mathbf{R}}_{22}^h\end{bmatrix}\begin{bmatrix}\tilde{\mathbf{h}}_x^i\\ \tilde{\mathbf{h}}_z^i\end{bmatrix} \tag{S7}
$$

with

$$
\left[\overline{\mathbf{\Theta}}_{\circ\,\text{-}}\right] = \begin{bmatrix}\Theta_{\circ\,\text{-}}^{(-N,-N)} & \dots\Theta_{\circ\,\text{-}}^{(-N,0)} & \dots & \Theta_{\circ\,\text{-}}^{(-N,N)}\\ \vdots & \vdots & \vdots & \\ \Theta_{\circ\,\text{-}}^{(0,-N)} & \dots\Theta_{\circ\,\text{-}}^{(0,0)} & \dots & \Theta_{\circ\,\text{-}}^{(0,N)}\\ \vdots & \vdots & \vdots & \\ \Theta_{\circ\,\text{-}}^{(N,-N)} & \dots\Theta_{\circ\,\text{-}}^{(N,0)} & \dots & \Theta_{\circ\,\text{-}}^{(N,N)}\end{bmatrix}. \tag{S8}
$$

Here, $\overline{\mathbf{\Theta}}_{\circ\,\text{-}} = \overline{\mathbf{R}}_{\circ\,\text{-}}^q$, where $\nu, \mu = 1, 2$, and $q = e, h$. $\overline{\mathbf{R}}^e$ and $\overline{\mathbf{R}}^h$ (with a size $[4N+2]\times[4N+2]$) characterize the generalized reflection for the fields viewed from the cavity region as shown in Fig.1a of the main text (throughout the paper the overlined symbols indicate matrices). The y components of the reflected field follow from Maxwell equations.

REFERENCES

1. K. Watanabe, "Numerical integration schemes used on the differential theory for anisotropic gratings," J. Opt. Soc. Am. A **19**, 2245-2252 (2002).
2. V. Jandieri, P. Baccarelli, G. Valerio, and G. Schettini, "1-D periodic lattice sums for complex and leaky waves in 2-D structures using higher order Ewald formulation," IEEE Trans. Antennas Propag. **67**, 2364-2378 (2019).
3. K. Yasumoto, *Electromagnetic Theory and Applications for Photonic Crystals* (Boca Raton, FL: CRC Press, 2005).